

# APEX-CHAMP<sup>+</sup> high-*J* CO observations of low-mass young stellar objects: I. The HH 46 envelope and outflow

T.A. van Kempen<sup>1,2</sup>, E.F. van Dishoeck<sup>1,3</sup>, R. Güsten<sup>4</sup>, L.E. Kristensen<sup>1</sup>, P. Schilke<sup>4</sup>, M.R. Hogerheijde<sup>1</sup>, W. Boland<sup>1,5</sup>,  
B. Nefs<sup>1</sup>, K.M. Menten<sup>4</sup>, A. Baryshev<sup>6</sup>, and F. Wyrowski<sup>4</sup>

<sup>1</sup> Leiden Observatory, Leiden University, P.O. Box 9513, 2300 RA Leiden, The Netherlands

<sup>2</sup> Center for Astrophysics, 60 Garden Street, Cambridge, MA 02138, USA

<sup>3</sup> Max-Planck Institut für Extraterrestrische Physik (MPE), Giessenbachstr. 1, 85748 Garching, Germany

<sup>4</sup> Max Planck Institut für Radioastronomie, Auf dem Hügel 69, D-53121, Bonn, Germany

<sup>5</sup> Nederlandse Onderzoeksschool Voor Astronomie (NOVA), P.O. Box 9513, 2300 RA Leiden, The Netherlands

<sup>6</sup> SRON Netherlands Institute for Space Research, P.O. Box 800, 9700 AV Groningen, The Netherlands

e-mail: tvankempen@cfa.harvard.edu

Draft: 0.7 July 2008

## ABSTRACT

**Context.** The spectacular outflow of HH 46/47 is driven by HH 46 IRS 1, an embedded Class I Young Stellar Object (YSO). Although much is known about this region from extensive optical and infrared observations, the properties of its protostellar envelope and molecular outflow are poorly constrained.

**Aims.** Our aim is to characterize the size, mass, density and temperature profiles of the protostellar envelope of HH 46 IRS 1 and its surrounding cloud material as well as the effect the outflow has on its environment.

**Methods.** The newly commissioned CHAMP<sup>+</sup> and LABOCA arrays on the APEX telescope, combined with lower frequency line receivers, are used to obtain a large ( $5' \times 5'$ ,  $0.6 \times 0.6$  pc) continuum map and smaller ( $80'' \times 80''$ ,  $36,000 \times 36,000$  AU) heterodyne maps in various isotopologues of CO and HCO<sup>+</sup>. The high-*J* lines of CO (6–5 and 7–6) and its isotopologues together with [C I] 2–1, observed with CHAMP<sup>+</sup>, are used to probe the warm molecular gas in the inner few hundred AU and in the outflowing gas. The data are interpreted with continuum and line radiative transfer models.

**Results.** Broad outflow wings are seen in CO low- and high-*J* lines at several positions, constraining the gas temperatures to a constant value of  $\sim 100$  K along the red outflow axis and to  $\sim 60$  K for the blue outflow. The derived outflow mass is of order  $0.4$ – $0.8$   $M_{\odot}$ , significantly higher than previously found. The bulk of the strong high-*J* CO line emission has a surprisingly narrow width, however, even at outflow positions. These lines cannot be fit by a passively heated model of the HH 46 IRS envelope. We propose that it originates from photon heating of the outflow cavity walls by ultraviolet photons originating in outflow shocks and the accretion disk boundary layers. At the position of the bow shock itself, the UV photons are energetic enough to dissociate CO. The envelope mass of  $\sim 5$   $M_{\odot}$  is strongly concentrated towards HH 46 IRS with a density power law of  $-1.8$ .

**Conclusions.** The fast mapping speed offered by CHAMP<sup>+</sup> allows the use of high-*J* CO lines and their isotopes to generate new insights into the physics of the interplay between the molecular outflow and protostellar envelope around low-mass protostars. The UV radiation inferred from the high-*J* CO and [C I] data will affect the chemistry of other species.

## 1. Introduction

The Young Stellar Object (YSO) HH 46 IRS 1 (RA=08h25m43.9s, Dec=−51d00h36s (J2000)), located at the edge of an isolated Bok Globule ( $D = 450$  pc) in the southern hemisphere (Schwartz 1977), is well-known for its spectacular outflow (Reipurth & Heathcote 1991), observed at both visible and infrared (IR) wavelengths with the *Hubble* and *Spitzer* Space Telescopes (e.g., Heathcote et al. 1996, Stanke et al. 1999, Noriega-Crespo et al. 2004, Velusamy et al. 2007). Deep H $\alpha$  observations using the VLT have revealed bow shocks associated with the HH 46 outflow up to a parsec away from the central source (Stanke et al. 1999). Its blue-shifted lobe expands outside the cloud in a low density region, due to the close proximity of the protostar to the edge of the cloud. Proper motion and radial velocity studies show that the outflow has an inclination of  $35^\circ$  with respect to the plane of the sky and flow velocities in atomic lines up to  $300$  km s<sup>−1</sup> (Dopita et al. 1982,

Reipurth & Heathcote 1991, Micono et al. 1998). The internal driving source was found to be HH 46 IRS 1 ( $L = 16$   $L_{\odot}$ ), an embedded Class I YSO (Raymond et al. 1994, Schwartz & Greene 2003). Surprisingly, much less is known about the properties of the protostellar envelope and the molecular outflow. Chernin & Masson (1991) and Olberg et al. (1992) mapped this region using low excitation CO lines, which show that contrary to the optical flows, the red-shifted outflow lobe is much stronger than the blue-shifted one. Chernin & Masson (1991) theorised that a lack of dense material in the path of the blue-shifted flow is responsible for this.

Comparisons between dust emission and molecular lines at submillimeter wavelengths, together with self-consistent radiative transfer calculations, have been extensively used to characterize the physical and chemical structure of Class 0 and Class I envelopes (Schöier et al. 2002, Jørgensen et al. 2002; 2005b, Maret et al. 2004). However, an essential component could not be probed with those data. The amount of warm ( $T > 50$  K) gas within the protostellar envelope as well as the influence of the

molecular outflow have not been constrained directly using observations of lower excited molecular lines in the 200 and 300 GHz bands. Although more complex molecules, such as  $\text{H}_2\text{CO}$  and  $\text{CH}_3\text{OH}$  emit at these frequencies from high energy levels (e.g. van Dishoeck et al. 1995, Ceccarelli et al. 2000), their more complex chemistry complicates their use as probes of the warm gas. Observations of CO at higher energies (up to 200 K) provide more reliable probes into the inner regions of envelopes and molecular outflows, but such lines have only been observed for a handful of sources (e.g., Hogerheijde et al. 1998, Parise et al. 2006, van Kempen et al. 2006). [C I] emission provides an important constraint on the strength of the radiation field within the outflows (Walker et al. 1993).

With the commissioning of the *Atacama Pathfinder Experiment* (APEX)<sup>1</sup> (Güsten et al. 2006), the CHAMP<sup>+</sup> instrument (Kasemann et al. 2006, Güsten et al. 2008) allows observations of molecular emission lines in the higher frequency sub-millimeter bands of southern sources, like HH 46. CHAMP<sup>+</sup> is the first array of its kind. With its 14 pixels, it is able to observe simultaneously in the 690 and 800 GHz atmospheric windows. This combination of dual-frequency observing and fast mapping speed, supplemented by lower frequency single pixel data and a LABOCA continuum array map (Kreysa et al. 2003, Siringo et al. 2008), provides a large range of highly complementary tracers of both the gas and dust conditions in the inner and outer regions of the envelope, as well as the molecular outflow on scales of a few arcminutes. Spectral line maps provide key information that is essential in the analysis of embedded YSOs which single-pointed observations cannot offer (Boogert et al. 2002, van Kempen et al. 2008).

In this paper, we present first results from CHAMP<sup>+</sup> and LABOCA observations of the HH 46 IRS 1 source, supplemented by lower frequency line receivers. Observations of highly excited CO,  $\text{HCO}^+$  and their isotopologues are used to constrain the properties of the protostellar envelope and molecular outflow of HH 46. In § 2 the observations performed at APEX are presented. Resulting spectra and maps can be found in § 3. In § 4 and 5 the protostellar envelope, molecular outflow and close surrounding of HH 46 are characterized using a radiative transfer analysis. In addition, we discuss a possible scenario for the high- $J$  CO emission in § 6. The final conclusions are given in § 7. CHAMP<sup>+</sup> observations of a larger sample of low-mass protostars are presented in a subsequent paper (van Kempen et al. submitted).

## 2. Observations

Molecular line observations were carried out with the CHAMP<sup>+</sup> array (Kasemann et al. 2006) of CO and its isotopologues, ranging in transitions from  $J=6-5$  to  $J=8-7$ , as well as [C I] 2–1. These observations were supplemented with low excitation line observations using APEX-1 (230 GHz, CO 2–1), APEX-2a (345 GHz, CO,  $\text{C}^{18}\text{O}$  and  $^{13}\text{CO}$  3–2, and  $\text{HCO}^+$  and  $\text{H}^{13}\text{CO}^+$  4–3) and FLASH (460 GHz, CO and  $^{13}\text{CO}$  4–3). In addition, LABOCA was used to map the entire region at 870  $\mu\text{m}$ . See Table 1 for an overview of the observed emission lines for each instrument and the corresponding rest frequencies and upper level ener-

gies, together with their corresponding APEX beams. All observations were done under excellent weather conditions with typical system temperatures of 2100 K for CHAMP<sup>+</sup>-I (SSB, 690 GHz), 7500 K for CHAMP<sup>+</sup>-II (SSB, 800 GHz), 1100 K for FLASH-I (DSB, 460 GHz), 290 K for APEX-1 and 230 K for APEX-2a (both SSB). Calibration errors are estimated at 15 to 20 %. The HH 46 protostar was spectrally mapped in CO 2–1, 3–2, 4–3, 6–5, 7–6 and  $\text{HCO}^+$  4–3, as well as  $^{13}\text{CO}$  6–5 and [C I] 2–1. The mapped area differs per line, ranging from  $40'' \times 40''$  for CO 4–3 to  $200'' \times 200''$  for CO 2–1, with most other lines covering  $80'' \times 80''$ . Observations were taken over a period of 2 years from July 2006 to September 2008 using Fast Fourier Transform Spectrometer (FFTS) (Klein et al. 2006) backends for all instruments, except CHAMP<sup>+</sup>, for which only the two central pixels were attached to the FFTS backends. Other CHAMP<sup>+</sup> pixels were attached to the MPI Array Correlator System (MACS) backends. FFTS backends are able to reach resolutions of 0.12 MHz ( $0.045 \text{ km s}^{-1}$  at 800 GHz), while the MACS units were used at a resolution of 1 MHz ( $0.36 \text{ km s}^{-1}$  at 800 GHz). Beam efficiencies are 0.75 for APEX-1, 0.73 for APEX-2a, 0.7 for FLASH-I, 0.56 for CHAMP<sup>+</sup>-I and 0.43 for CHAMP<sup>+</sup>-II. Pointing was checked on nearby sources and found to be accurate within  $3''$  for the APEX-2a observations. For CHAMP<sup>+</sup>, pointing is accurate within  $\sim 5''$ . All observations were taken using position switching with reference positions in azimuth ranging from  $600''$  to  $3600''$ .

LABOCA observed HH 46 during November 2007 using its 295 pixels in a spiral mode centered on the IR position using a position switch of  $600''$  arcseconds. Only the inner  $5' \times 5'$  of the  $11'$  field of view was used. The field was integrated down to a noise level of 0.01 Jy/beam, averaged over the entire region. Due to the used spiral mode, the map contains a radial increase of noise towards the edge of the map. The continuum data were reduced with the BOA package<sup>2</sup>.

## 3. Results

### 3.1. Single pixel spectra

Figure 1 shows the spectra taken at the position of HH 46 IRS 1 for all lines in Table 1. Integrated intensities, peak temperatures and estimated contributions from the blue- and red-shifted outflowing gas are given in Table 2. The latter are derived by subtracting the central part of the line profile, associated with the quiescent gas, with a single gaussian. Emission was detected for all lines with the exception of  $\text{C}^{18}\text{O}$  6–5 and  $^{13}\text{CO}$  8–7. The quiescent gas component peaks at a  $V_{\text{LSR}}$  of  $5.3 \pm 0.1 \text{ km s}^{-1}$  and has a FWHM of  $1-2 \text{ km s}^{-1}$  depending on the energy of the upper level. Since the detection of the [C I] 2–1 line is only  $3.5 \sigma$ , a gaussian fit is overplotted in Fig. 1.

Integrated intensities range from  $82.5 \text{ K km s}^{-1}$  for CO 3–2 to  $1.1 \text{ K km s}^{-1}$  for  $\text{H}^{13}\text{CO}^+$ . All  $^{12}\text{CO}$  line profiles show contributions of a red-shifted outflow lobe within the beam, including the high excitation CO 7–6 line. Emission from the blue-shifted outflow lobe is much weaker and not found for CO 7–6. In the other lines, outflow emission is only detected for  $\text{HCO}^+$  4–3, where a weak red-shifted wing is found.

### 3.2. Maps around IRS 1

The resulting dust emission map ( $5' \times 5'$ ) at 870  $\mu\text{m}$  is shown in Fig. 2. The envelope is clearly resolved, considering the beam-

<sup>1</sup> This publication is based on data acquired with the Atacama Pathfinder Experiment (APEX) in programs E-77.C-0217, X-77.C-0003, X-79.C-0101 and E-081.F-9837A. APEX is a collaboration between the Max-Planck-Institut für Radioastronomie, the European Southern Observatory, and the Onsala Space Observatory. APEX-1 was used during science verification in June 2008.

<sup>2</sup> <http://www.astro.uni-bonn.de/boawiki>

**Table 1.** Overview of the observations

| Mol.                            | Trans.<br>$J_u-J_l$ | $E_u$<br>(K) | Freq.<br>(GHz) | Instrument             | Beam<br>( $''$ ) | Map | Map Size             |
|---------------------------------|---------------------|--------------|----------------|------------------------|------------------|-----|----------------------|
| CO                              | 2-1                 | 16.6         | 230.538        | APEX-1                 | 28               | y   | $200'' \times 170''$ |
|                                 | 3-2                 | 33.2         | 345.796        | APEX-2a                | 18               | y   | $80'' \times 80''$   |
|                                 | 4-3                 | 55.3         | 461.041        | FLASH-I                | 14               | y   | $40'' \times 40''$   |
|                                 | 6-5                 | 116.2        | 691.473        | CHAMP <sup>+</sup> -I  | 9                | y   | $80'' \times 80''^a$ |
|                                 | 7-6                 | 154.8        | 806.651        | CHAMP <sup>+</sup> -II | 8                | y   | $80'' \times 80''$   |
| <sup>13</sup> CO                | 3-2                 | 31.7         | 330.588        | APEX-2a                | 18               | n   | -                    |
|                                 | 4-3                 | 52.9         | 440.765        | FLASH-I                | 14               | n   | -                    |
|                                 | 6-5                 | 111.1        | 661.067        | CHAMP <sup>+</sup> -I  | 9                | y   | $50'' \times 50''$   |
|                                 | 8-7                 | 190.4        | 881.273        | CHAMP <sup>+</sup> -II | 8                | n   | -                    |
| C <sup>18</sup> O               | 3-2                 | 31.6         | 329.331        | APEX-2a                | 18               | n   | -                    |
|                                 | 6-5                 | 110.6        | 658.553        | CHAMP <sup>+</sup> -I  | 9                | n   | -                    |
| [C I]                           | 2-1                 | 62.3         | 809.342        | CHAMP <sup>+</sup> -II | 8                | y   | $50'' \times 50''^a$ |
| HCO <sup>+</sup>                | 4-3                 | 42.8         | 356.724        | APEX-2a                | 18               | y   | $80'' \times 80''$   |
| H <sup>13</sup> CO <sup>+</sup> | 4-3                 | 41.6         | 346.998        | APEX-2a                | 18               | n   | -                    |
| 870 $\mu$ m continuum           |                     |              |                | LABOCA                 | 18               | y   | $6' \times 6'$       |

<sup>a</sup> additional mapping was performed in these lines around the bow shock position.

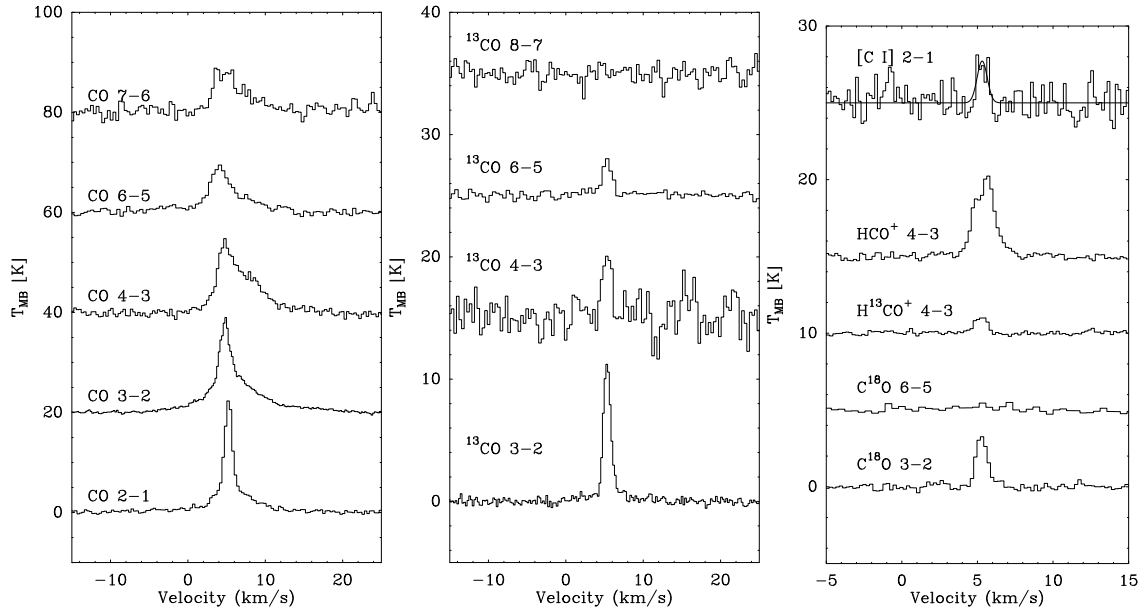


**Fig. 1.** Single spectra taken at the central position of HH 46 (all in order from *bottom to top*). *Left* : <sup>12</sup>CO 2-1, <sup>12</sup>CO 3-2, <sup>12</sup>CO 4-3, <sup>12</sup>CO 6-5 and <sup>12</sup>CO 7-6. *Middle* : <sup>13</sup>CO 3-2, <sup>13</sup>CO 4-3, <sup>13</sup>CO 6-5 and <sup>13</sup>CO 8-7. *Right* : C<sup>18</sup>O 3-2, C<sup>18</sup>O 6-5, H<sup>13</sup>CO<sup>+</sup> 4-3, HCO<sup>+</sup> 4-3 and [C I] 2-1. Spectra have been shifted vertically for easy viewing.

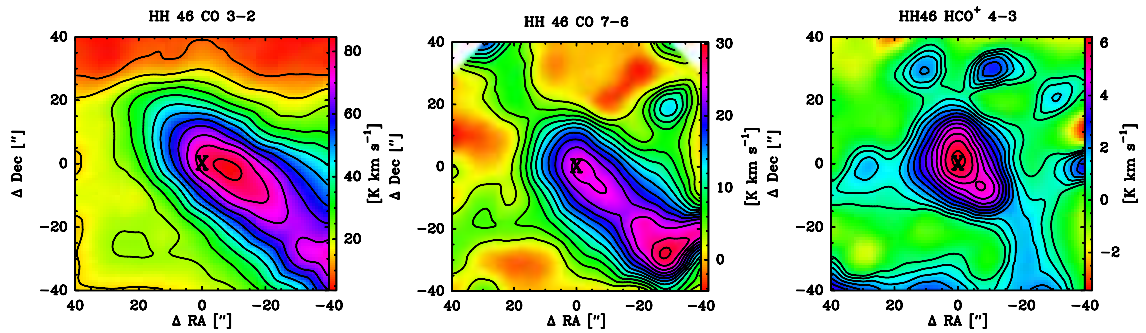


**Fig. 3.** From *left to right* : Spectrally integrated CO 3-2, 7-6 and HCO<sup>+</sup> 4-3 maps of HH 46 (see Table 2). Contour levels are at  $3\sigma$ ,  $6\sigma$ ,  $9\sigma$ , ... ( $\sigma = 1.5$  K for CO 3-2, 0.4 K for HCO<sup>+</sup> 4-3 and 0.8 K for CO 7-6). The position of the IR source is marked with a **X**. Note that the HCO<sup>+</sup> 4-3 map has higher noise levels than the central spectrum in Fig. 1.

size of  $18''$  of the APEX dish. The envelope is slightly elongated on a south-west to north-east axis. South of HH 46, dust emis-

**Table 2.** Observed molecular line intensities<sup>a</sup>.

| Line                            | Transition | Central position                                     |                          |                                |                                 | Envelope/outflow position <sup>b</sup>               |                          |
|---------------------------------|------------|--|--------------------------|--------------------------------|---------------------------------|--|--------------------------|
|                                 |            | $\int T_{\text{MB}} dV^c$<br>(K km s <sup>-1</sup> ) | $T_{\text{peak}}$<br>(K) | Red<br>(K km s <sup>-1</sup> ) | Blue<br>(K km s <sup>-1</sup> ) | $\int T_{\text{MB}} dV^c$<br>(K km s <sup>-1</sup> ) | $T_{\text{peak}}$<br>(K) |
| CO                              | 2–1        | 53.3   | 22.4                     | 11.5                           | 3.8                             | 61.7   | 21.2                     |
|                                 | 3–2        | 82.5   | 19.4                     | 28.0                           | 13.4                            | 65.6   | 19.8                     |
|                                 | 4–3        | 70.5   | 14.9                     | 44.2                           | 3.7                             | 38.5   | 14.0                     |
|                                 | 6–5        | 42.6   | 9.5                      | 11.7                           | 5.7                             | 34.6   | 8.8                      |
|                                 | 7–6        | 46.5   | 8.6                      | 17.6                           | <3.7                            | 25.3   | 5.9                      |
| <sup>13</sup> CO                | 3–2        | 14.3   | 11.4                     | -                              | -                               | -  | -                        |
|                                 | 4–3        | 8.0  | 5.5                      | -                              | -                               | -  | -                        |
|                                 | 6–5        | 3.9  | 2.9                      | -                              | -                               | <0.6 <sup>d</sup>                                    | -                        |
|                                 | 8–7        | -  | <0.9 <sup>c</sup>        | -                              | -                               | -  | -                        |
| C <sup>18</sup> O               | 3–2        | 3.2  | 3.3                      | -                              | -                               | -  | -                        |
|                                 | 6–5        | -  | <0.5 <sup>d</sup>        | -                              | -                               | -  | -                        |
| [C I]                           | 2–1        | 2.3  | 2.7                      | -                              | -                               | -  | <1.8 <sup>d</sup>        |
| HCO <sup>+</sup>                | 4–3        | 8.5  | 5.4                      | 1.4                            | -                               | -  | <0.9 <sup>d</sup>        |
| H <sup>13</sup> CO <sup>+</sup> | 4–3        | 1.1  | 1.0                      | -                              | -                               | -  | -                        |

<sup>a</sup> Red and Blue shifted emission are calculated by subtracting the central part of the line profile with a gaussian with FWHM of 1.5–2 km s<sup>-1</sup>.

<sup>b</sup> Position :  $\Delta\text{RA} = -20''$ ,  $\Delta\text{Dec} = -20''$ .

<sup>c</sup> Velocity range used for integration: -5 km s<sup>-1</sup> to 15 km s<sup>-1</sup>

<sup>d</sup> Upper limit of  $3\sigma$  in a 0.7 km s<sup>-1</sup> channel.

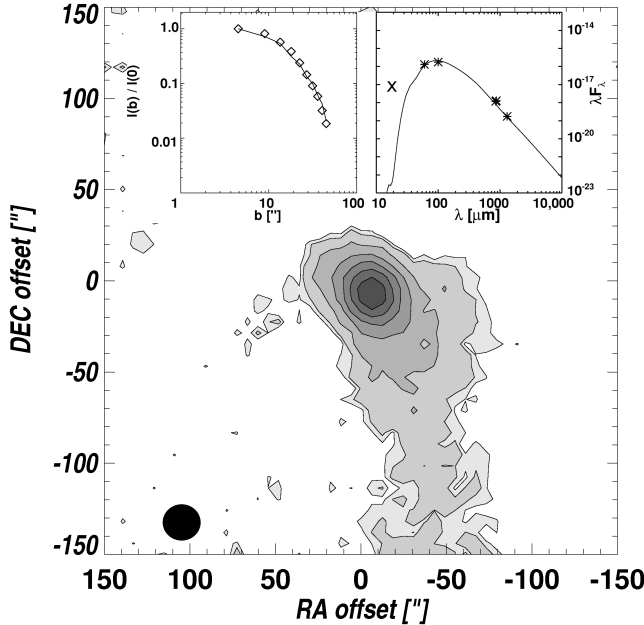


**Fig. 2.** Continuum map at 870  $\mu\text{m}$  of HH 46 obtained with LABOCA with contour levels plotted in multiples of the  $3\sigma$  noise level of 0.05 Jy/beam. *Left inset:* the radial profile going outwards from the IR position. *Right inset:* the SED from HH 46 from 10  $\mu\text{m}$  to 10 mm. In both panels, the best-fitting DUSTY model is overplotted.

sion from the cold cloud is seen. The total integrated flux in a 120'' diameter aperture around the source position is found to be 3.7 Jy. Reduction of archival SCUBA (850  $\mu\text{m}$ ) data of this region yielded a flux of 3.3 Jy (Di Francesco et al. 2008), a difference in flux well within the estimated calibration errors of both SCUBA and LABOCA. Using the formula in Shirley et al. (2000), the total mass in the 300'' mapped area of the cloud is 8

$M_{\odot}$ , while the central 120'' is associated with a mass of 3.7  $M_{\odot}$ , both with an assumed dust temperature of 20 K.

The integrated spectral line maps of CO 3–2, 7–6 and HCO<sup>+</sup> 4–3 (all 80'' × 80'') in Fig. 3 show a similar structure as the continuum maps (see also §5.4.1), although the elongation to the south-west is much more pronounced in the CO lines, with an integrated intensity of CO 3–2 of 65.6 K km s<sup>-1</sup> seen in the -20'', -20'' position. As can be seen from the red- and blue-shifted velocity maps of CO 2–1, 4–3 and 6–5 in Fig. 4, the shape of the integrated intensity maps is largely due to the outflow contributions, especially for the low-excitation lines, even in the CO 2–1 map, for which a map of 200'' × 200'' was observed. This is in agreement with the results from Chernin & Masson (1991). In fact, the CO 3–2 line is so prominent that it can contribute significantly to the ‘continuum’ emission seen by LABOCA. The CO 3–2 line produces a flux density of 40 mJy/beam off source, equivalent to the LABOCA  $4\sigma$  level. The total continuum emission seen at these positions is  $\sim 12$ – $15\sigma$ . CO emission may thus contribute up to 30% to the observed LABOCA emission in the outflow region. Another possible contribution to the dust emission at 870  $\mu\text{m}$  is heating of the dust grains by UV radiation that takes place in the cavity walls. This is further discussed in § 6.

In contrast, the elongation in the HCO<sup>+</sup> 4–3 map is much less pronounced than in the CO low- $J$  data. The map of [C I] 2–1 is not shown, since no lines were detected down to 1.8 K ( $3\sigma$ ), except at the source position (Fig. 1) and at the bow shock (see § 3.3). In the map of <sup>13</sup>CO 6–5, lines are only detected at the central position and at neighbouring pixels along the outflow.

Fig. 5 shows the total distribution of <sup>12</sup>CO 6–5 over the entire area, overplotted over the Spitzer image of Noriega-Crespo et al. (2004) with the Spitzer-IRAC 1, 2 and 4 bands (3.6, 4.5 and 8.0  $\mu\text{m}$  respectively.) The CO 6–5 integrated intensities follow the outflow but do not extend all the way out to the bow shock. In addition, several maximum intensities can be found. The first one corresponds with the protostellar envelope, but the other two seem to be related to the outflow. Similarly regularly spaced ‘knots’ are seen in, for example, the CO 3–2 maps of the NGC 1333 IRAS4A outflow (Blake et al. 1995).

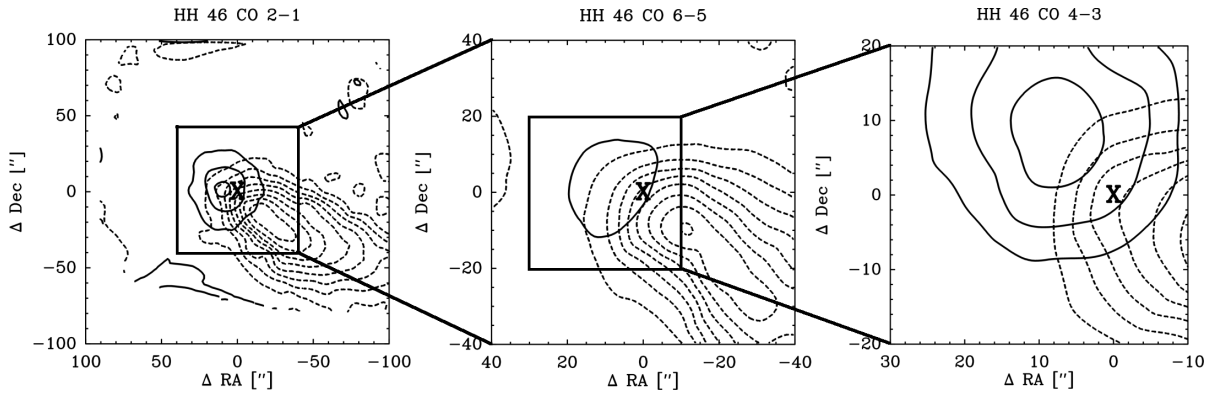


**Fig. 4.** Maps of HH 46 showing the outflowing gas. Solid lines show blue-shifted, dashed lines show red-shifted emission. Contours are drawn at  $3\sigma$ ,  $6\sigma$ ,  $9\sigma$ , ..., with the exception of CO 2–1, where contours are drawn  $3\sigma$ ,  $9\sigma$ ,  $15\sigma$ , ... .  $3\sigma$  levels are  $0.4 \text{ K km s}^{-1}$ ,  $1 \text{ K km s}^{-1}$  and  $1 \text{ K km s}^{-1}$  for 2–1, 6–5 and 4–3 respectively. Blue- and red-shifted emission is derived by subtracting a central gaussian fitted to the quiescent central part of the line profiles. Velocities typically range from  $-5$  to  $1.5 \text{ km s}^{-1}$  for the blue-shifted emission and  $8$  to  $15 \text{ km s}^{-1}$  for the red-shifted. Note that the images are at different spatial scales and progressively zoom in onto the central protostar from left to right. The position of the infrared source is marked in all maps with a ‘X’.

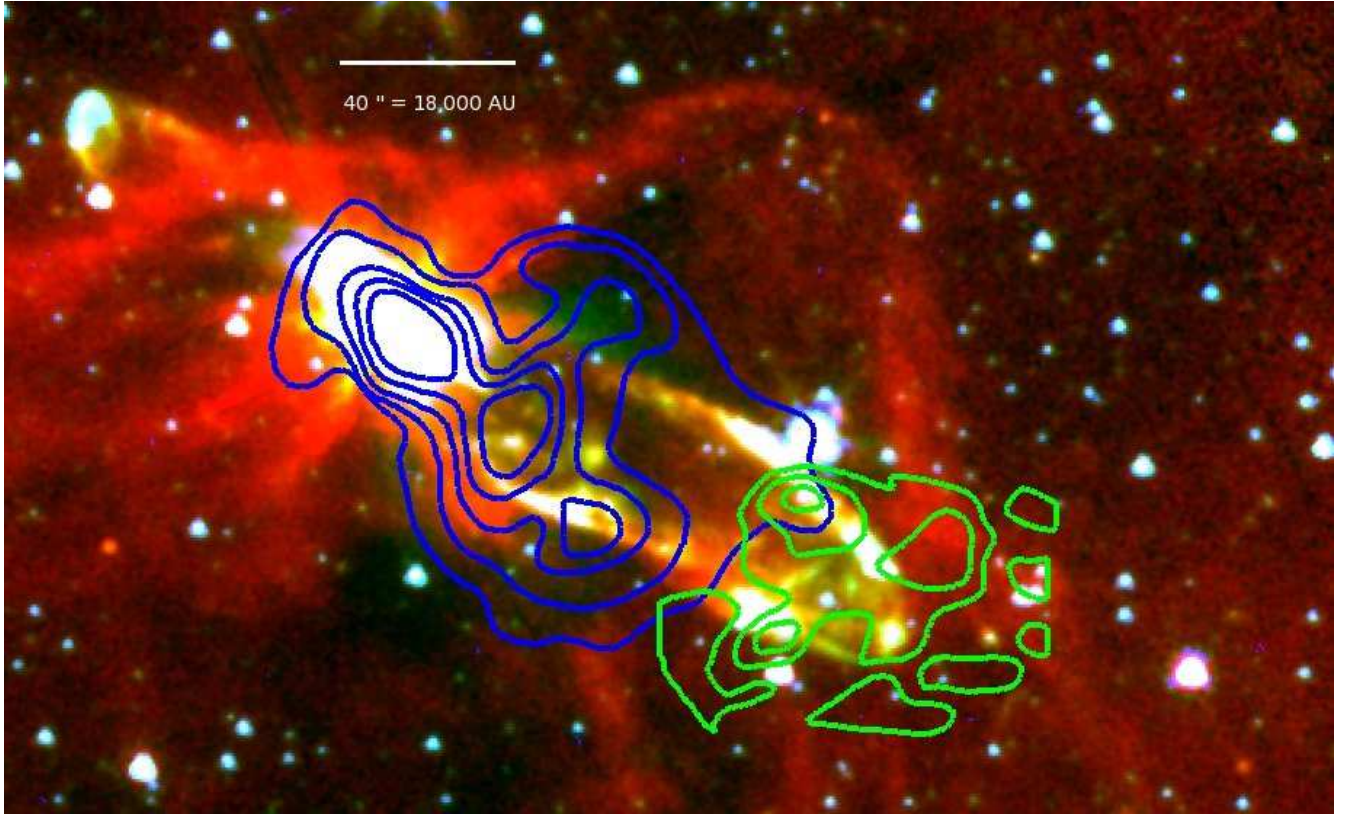


**Fig. 5.** The integrated intensity of CO 6–5 (blue contours) and [C I] 2–1 (green contours) overplotted on the Spitzer-IRAC 1 (blue), 2 (green) and 4 (red) bands of the entire HH46 region. CO 6–5 contours are in increasing order of  $5 \text{ K km s}^{-1}$ . The clear cut between the CO and [C I] emission near the bow shock suggests that UV photons capable of dissociating CO are present near the bow shock.

Figure 6 shows the observed spectra within the central  $80'' \times 80''$  of CO 3–2, taken with APEX-2a, and CO 6–5, taken with CHAMP<sup>+</sup>-I. Both are binned to square  $10'' \times 10''$  pixels. The line profiles show an interesting distribution of emission, especially at the positions associated with the outflowing gas. The CO 3–2 spectra consist of a central gaussian originating in the cold envelope material surrounding the protostar, with a strong red-shifted outflow of up to  $10 \text{ km s}^{-1}$  away from the source and

cloud velocity in the south-east direction. The line profile at the source position has a quiescent component, flanked by both red- and blue-shifted emission. Interestingly, the CO 6–5 emission shows a quiescent component with relatively weak red-shifted emission at other positions in the map. The central part of the line profile can be fitted with narrow ( $\Delta V = 2\text{--}3 \text{ km s}^{-1}$ ) gaussian profiles. At the central position, outflow emission in the CO 6–5

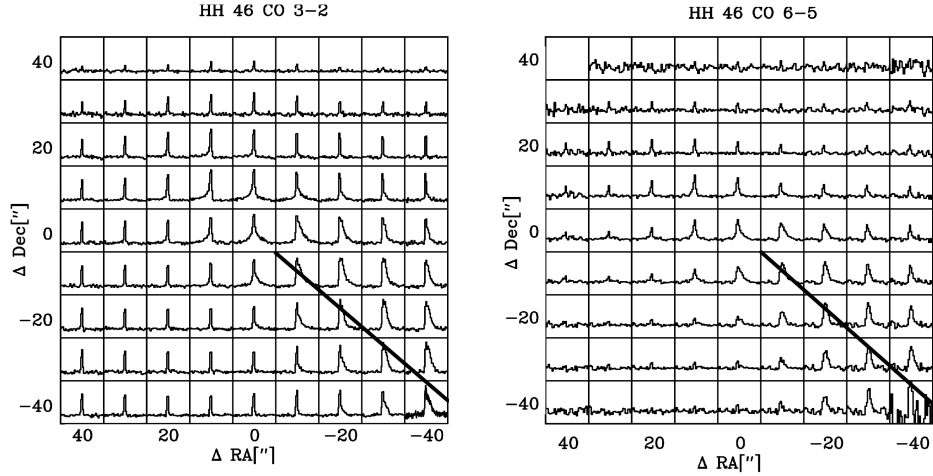


**Fig. 6.** Spectra of HH 46 of CO 3–2 (left) and CO 6–5 (right) in the  $80'' \times 80''$  mapping area. Individual spectra are shown on a  $T_{\text{MB}}$  scale of -5 to 20 K for CO 3–2 and from -3 to 12 K for CO 6–5. Both axes are from -10 to 20  $\text{km s}^{-1}$ . The black lines show the axis of the red outflow.

line is much more prominent, but a strong quiescent component is still present.

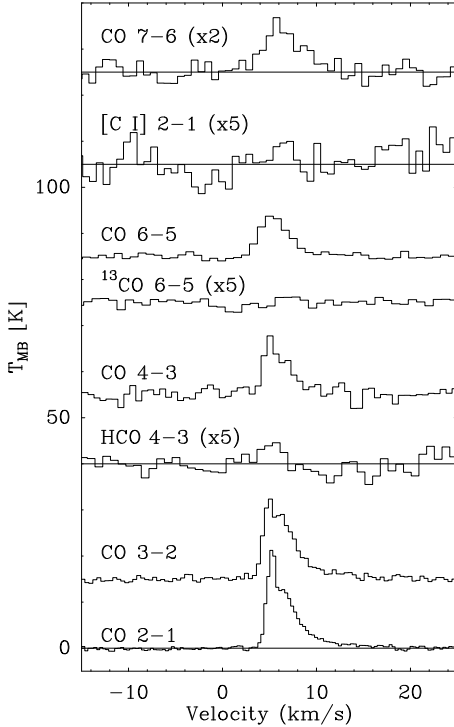


**Fig. 7.** Single spectra of (from bottom to top): CO 2–1, CO 3–2,  $\text{HCO}^+$  4–3, CO 4–3,  $^{13}\text{CO}$  6–5, CO 6–5, [C I] 2–1 and CO 7–6. All spectra are at an position in the red outflow lobe of  $\Delta\text{RA} = -20''$  and  $\Delta\text{Dec} = -20''$ . The quiescent gas has a FWHM of 1.5  $\text{km s}^{-1}$  centered at 5.3  $\text{km s}^{-1}$ .

Figure 7 shows all spectra observed within the spectral line maps at a relative position of  $(-20'', -20'')$ . Peak temperatures and integrated intensities are given in Table 2. This position covers the red-shifted outflow seen prominently in the emission of

the low-excitation CO 3–2 and 2–1 lines. Even CO 4–3 shows significant red-shifted outflow emission. The outflowing gas is still present in the high- $J$  CO lines. However, for both CO 6–5 and 7–6 a significant part of the emission (on the order of 70–80%) originates in a quiescent narrow component. The isotopologue  $^{13}\text{CO}$  6–5 is not detected, down to a  $3\sigma$  level of 0.6 K in a 0.7  $\text{km s}^{-1}$  bin. Similarly, no [C I] is detected down to 1.8 K and no  $\text{HCO}^+$  4–3 is detected down to 0.9 K, both  $3\sigma$  in a 0.7  $\text{km s}^{-1}$  bin.

Using the limits on the  $^{13}\text{CO}$  6–5 emission at both the central position and the selected off-position, it is found that the quiescent component at the central position is optically thick ( $\tau > 3$ ), while the quiescent emission at the outflow position is optically thin ( $\tau < 0.4$ ), as no  $^{13}\text{CO}$  is detected between 0 and 10  $\text{km s}^{-1}$ . This analysis assumes a  $^{12}\text{CO}:^{13}\text{CO}$  ratio of 70:1 (Wilson & Rood 1994).

Although outflow emission heavily influences the line profiles of the CO 3–2 and 6–5 throughout the maps, positions south, south-east, and north of the (0,0) position are not affected by any outflowing gas, as seen in Fig. 6. About  $30''$  to  $40''$  north of HH 46, both the CO 3–2 and CO 6–5 are not detected. Even in the map of CO 2–1, no emission was found at these positions. It is concluded that the cold cloud material of the surrounding Bok globule does not extend to these scales. At positions south and south-east of HH 46, CO 3–2 emission is seen, but no CO 6–5 is detected there.

### 3.3. Bow shock

The bow shock associated with the red outflow lobe is clearly visible in the IR images of Noriega-Crespo et al. (2004), located at a relative offset of  $(-100'', -60'')$  with respect to the source. Additional observations of this bow shock in CO 6–5, [C I] 2–1 and  $^{13}\text{CO}$  6–5 were carried out over a  $90''$  by  $60''$  area. Fig. 5 shows the distribution of [C I] 2–1 emission in this region. Narrow [C I] 2–1 is clearly detected near and at the position of the bow shock, where it has a integrated intensity of 1.2  $\text{K km s}^{-1}$  with a peak temperature of 1.7 K. Interestingly, the emission seems to be spatially extended along the outflow axis into the outflow lobe. No  $^{13}\text{CO}$  6–5 was detected at any position near the



bow shock down to an rms of 85 mK in a  $0.3 \text{ km s}^{-1}$  bin. The combination of detected [C I] 2–1 and lack of CO 6–5 emission suggests that CO is dissociated by either the shocks present near the bow shock or by UV photons capable of dissociating CO (see § 6.1).

## 4. Envelope and surrounding cloud

### 4.1. Envelope - dust

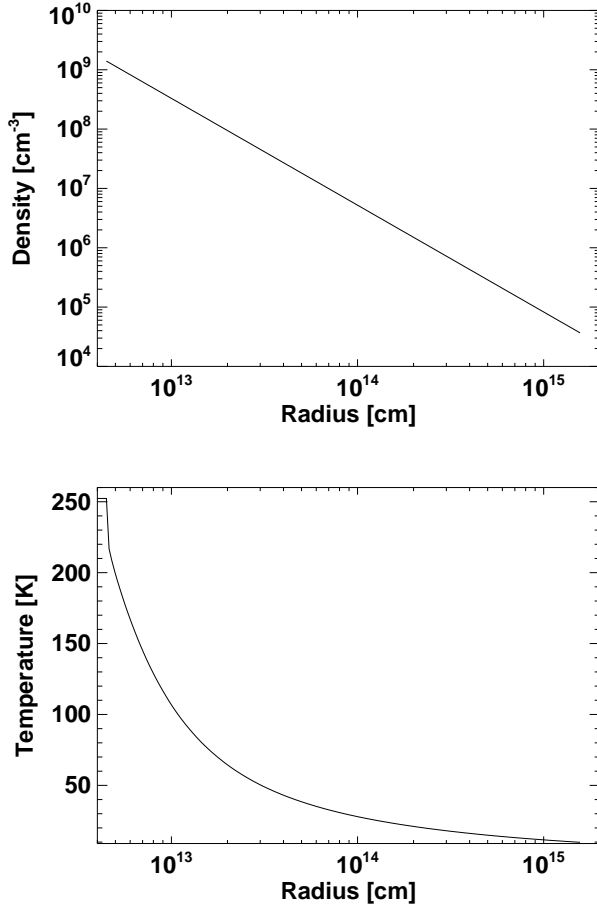


**Fig. 8.** The density (*left*) and temperature (*right*) distributions of the DUSTY modelling of HH 46.

Using the 1-D radiative transfer code DUSTY (Ivezić & Elitzur 1997), a spherically symmetric envelope model is constructed by fitting the radial profile of the  $870 \mu\text{m}$  image and the SED simultaneously, determining the size, total mass, inner radius as well as density and temperature profiles of the protostellar envelope. For a more thorough discussion of this method, see Jørgensen et al. (2002). DUSTY uses  $Y$  ( $=R_{\text{outer}}/R_{\text{inner}}$ ),  $p$ , the power law exponent of the density gradient ( $n \propto r^{-p}$ ), and  $\tau_{100}$ , the opacity at  $100 \mu\text{m}$  as its free parameters. The temperature at the inner boundary was taken to be 250 K. For the SED, fluxes were used at  $60$  and  $100 \mu\text{m}$  (IRAS, Henning et al. 1993),  $850 \mu\text{m}$  (SCUBA archive, Di Francesco et al. 2008),  $870 \mu\text{m}$  (LABOCA, this work) and  $1.3 \text{ mm}$  (SEST Henning et al. 1993). No emission from MIPS at  $24 \mu\text{m}$  or ISO-SWS (Nisini et al. 2002, Noriega-Crespo et al.

2004) was used. The  $24 \mu\text{m}$  flux is included in the figure as reference. Note that the model is unable to account for this high flux. Deviations from spherical symmetry (outflow cavities), additional shock emission (Velusamy et al. 2007) or larger inner holes (Jørgensen et al. 2005a) are often inferred to explain the observed high mid-IR fluxes that cannot be fitted with DUSTY. The radial profile was determined in directions away from the southwest outflow and cloud material, ignoring any emission in a  $90^\circ$  cone to the south-west. Results for the best-fitting envelope model to the  $16 L_\odot$  for the source luminosity can be found in Table 3. Temperature and density distributions are displayed in Figure 8. The corresponding fits are shown in the insets of Fig. 2.

The envelope contains a large amount of cold gas ( $\sim 5.1 M_\odot$ ) within the outer radius of  $20,800 \text{ AU}$  ( $\sim 0.1 \text{ pc}$ ), but with a significant fraction of the mass concentrated towards the inner envelope due to the steep density profile ( $p=1.8$ ). The  $\text{H}_2$  density at  $1,000 \text{ AU}$  is  $2.4 \times 10^6 \text{ cm}^{-3}$ . The transition from envelope to parental cloud is not taken into account.

**Table 3.** Results from radiative transfer modelling for envelope properties

| Best fit     |     | Envelope Properties                |                                   |
|--------------|-----|------------------------------------|-----------------------------------|
| $Y$          | 700 | $R_{\text{inner}} (250 \text{ K})$ | 30 AU                             |
| $p$          | 1.8 | $R(30 \text{ K})$                  | 533 AU                            |
| $\tau_{100}$ | 2.6 | $R(n_{\text{de}})$                 | 6,100 AU                          |
|              |     | $R_{\text{outer}}$                 | 20,800 AU                         |
|              |     | $n(1000 \text{ AU})$               | $2.5 \times 10^6 \text{ cm}^{-3}$ |
|              |     | $M_{\text{env}} (> 10 \text{ K})$  | $5.1 M_\odot$                     |

### 4.2. Envelope - gas

The physical structure of the gas is best traced by optically thin emission that probes the quiescent envelope gas at high density (Jørgensen et al. 2005b). To that end, the temperature and density structure derived from the dust radiative transfer model was used as a model input for the model using the RATRAN radiative transfer code (Hogerheijde & van der Tak 2000) with data files from the LAMDA database (Schöier et al. 2005). Two different scenarios were investigated. In the first, only freeze-out is taken into account, with an inner CO abundance  $X_0$  of  $2.7 \times 10^{-4}$  with respect to  $\text{H}_2$  and an outer CO abundance  $X_d$  of  $10^{-5}$ . In the second, the abundances are the same, except that a high abundance  $X_0 = 2.7 \times 10^{-4}$  has been adopted for the outermost envelope regions where density is lower than  $n_{\text{de}} = 10^5 \text{ cm}^{-3}$ . This so-called 'drop' abundance profile is motivated by the fact that at low densities, the timescales for freeze-out onto the grains are longer than the typical lifetimes of the cores of a few  $10^5 \text{ yr}$ . The abundances  $X_0$  and  $X_d$  were derived by Jørgensen et al. (2002) and Jørgensen et al. (2005b) for a range of sources, based on emission from optically thin lines. Isotope ratios were taken from Wilson & Rood (1994) of 550 for  $\text{CO}:\text{C}^{18}\text{O}$  and 70 for  $\text{CO}:\text{C}^{13}\text{CO}$ . The velocity field of the envelope is represented by a turbulent width of  $0.8 \text{ km s}^{-1}$ . The gas and dust temperature were assumed to couple throughout the envelope. Gas and dust temperatures decouple in the cold outer envelope region with the gas temperature dropping by a factor two with respect to the dust temperature (Ceccarelli et al. 1996, Doty & Neufeld 1997). This drop can be counteracted, however, by UV radiation from the outside impinging on the envelope and heating the gas. For a

more thorough discussion, see also Jørgensen et al. (2002). Any small temperature difference in the outer envelope affect mostly the low- $J$   $^{12}\text{CO}$  lines.

Table 4 gives the results for these models. For each model, the envelope contribution of both  $\int T_{\text{MB}}$  and  $T_{\text{peak}}$  are given. The optically thin lines ( $\text{C}^{18}\text{O}$  3–2 and 6–5, as well as the  $^{13}\text{CO}$  8–7) show that the inclusion of a higher abundance outer layer, as in a drop model, is necessary to increase the  $\text{C}^{18}\text{O}$  3–2 emission to the observed levels. At the same time this does not change the emission of the  $\text{C}^{18}\text{O}$  6–5 line. The adopted abundances of the drop abundance (Model 2) agree best with the observed intensities of the optically thin lines, including the upper limits on  $\text{C}^{18}\text{O}$  6–5 and  $^{13}\text{CO}$  8–7 within the uncertainties.

**Table 4.** Results from molecular line radiative transfer modelling.

| Line                           | Model 1 <sup>a</sup> |                     | Model 2 <sup>a</sup> |                     | Obs.              |
|--------------------------------|----------------------|---------------------|----------------------|---------------------|-------------------|
|                                | $\int T_{\text{MB}}$ | $T_{\text{peak}}^b$ | $\int T_{\text{MB}}$ | $T_{\text{peak}}^b$ | $T_{\text{peak}}$ |
| CO 2–1                         | 9.4                  | 5.0/22.2            | 10.4                 | 4.5/78.9            | 22.4              |
| CO 3–2                         | 8.0                  | 4.7/22.5            | 7.1                  | 3.8/55.8            | 19.4              |
| CO 4–3                         | 7.3                  | 4.2/16.9            | 4.7                  | 3.1/47.3            | 14.9              |
| CO 6–5                         | 6.8                  | 3.4/4.8             | 5.1                  | 2.7/5.2             | 9.5               |
| CO 7–6                         | 4.1                  | 2.2                 | 4.0                  | 2.2                 | 8.6               |
| $^{13}\text{CO}$ 3–2           | 4.6                  | 3.7/3.8             | 5.9                  | 3.6/10.7            | 11.4              |
| $^{13}\text{CO}$ 4–3           | 3.5                  | 2.8                 | 4.2                  | 2.6/3.8             | 5.5               |
| $^{13}\text{CO}$ 6–5           | 1.9                  | 1.2                 | 1.9                  | 1.2                 | 2.9               |
| $^{13}\text{CO}$ 8–7           | 0.8                  | 0.5                 | 0.8                  | 0.5                 | <0.9              |
| $\text{C}^{18}\text{O}$ 3–2    | 1.3                  | 1.2                 | 3.5                  | 2.9                 | 3.3               |
| $\text{C}^{18}\text{O}$ 6–5    | 1.0                  | 0.7                 | 1.0                  | 0.7                 | <0.5              |
| $\text{HCO}^+$ 4–3             | 3.5                  | 2.3/11.8            | 2.8                  | 2.5/8.3             | 5.4               |
| $\text{H}^{13}\text{CO}^+$ 4–3 | 0.75                 | 0.7                 | 0.75                 | 0.7                 | 1.0               |

<sup>a</sup> Model 1 has a jump abundance profile with  $X_0/X_d$  of  $2.7 \times 10^{-4}/1 \times 10^{-5}$ . Model 2 has a drop abundance profile with  $X_0/X_d/X_0$  of  $2.7 \times 10^{-4}/1 \times 10^{-5}/2.7 \times 10^{-4}$ .

<sup>b</sup> For some lines, the peak temperature is given as X/Y. The first value is the actual  $T_{\text{peak}}$  in the model profile. The second value refers to the peak of a gaussian fitted to the line wings of model profiles which show self-absorption. If only a single number is given, the modelled line is gaussian in nature and does not have self-absorption.

<sup>c</sup>  $\text{HCO}^+$  abundances of  $X_0$  and  $X_d$  are  $2.0 \times 10^{-8}$  and  $3.0 \times 10^{-9}$ .

The very optically thick low- $J$   $^{12}\text{CO}$  (2–1, 3–2 and 4–3) lines cannot be fitted by either model due to the lack of self-absorption in the observed lines, which is strongly present in the modelled profiles. To obtain a rough correction for self-absorption, gaussian fits were made to the line wings of CO, similar to the one in van Kempen et al. submitted.. Such gaussian fits provide only upper limits to the peak emission of CO, as the true CO emission is best fitted with an infall velocity (Schöier et al. 2002).

Even with gaussian fits, the high- $J$  (6–5 and higher) lines of both  $^{13}\text{CO}$  and  $^{12}\text{CO}$  are severely underproduced by almost a factor 3. Note that their model line profiles do not show self-absorption. The emission in these lines is almost identical in the drop or jump abundance models. Increasing or decreasing the CO abundances  $X_0$  and  $X_d$  is not possible since the emission of optically thin lines such as  $\text{C}^{18}\text{O}$  6–5 and 3–2 would then either be over- or underestimated. The main conclusion from the envelope models is therefore that an additional, relatively optically thin but hot component unobscured by the warm envelope region is needed to account for this emission. The origin of this hot component producing narrow highly excited CO line emission will be discussed in § 5.6.

The integrated [C I] 2–1 intensity ( $2.3 \text{ K km s}^{-1}$ ) can be reproduced with a constant abundance ratio  $\text{C}/\text{H}_2$  of  $3\text{--}5 \times 10^{-7}$  (or about 0.1–3% of CO, depending on radius), typical for the densest molecular clouds. The [C I] line is optically thin, even for much higher abundances. A C abundance as high as  $5 \times 10^{-6}$  can be maintained by photodissociation of CO due to cosmic-ray induced UV photons deep inside the envelope (e.g., Flower et al. 1994).

$\text{HCO}^+$  4–3 shows little to no difference between Model 1 and 2, because most of the emission traces gas denser than  $10^5 \text{ cm}^{-3}$ . There is a significant difference in  $T_{\text{peak}}$  from the line profile vs. gaussian fits for main isotope line because of self-absorption. The optically thin  $\text{H}^{13}\text{CO}^+$  is slightly underproduced, similar to the  $\text{C}^{18}\text{O}$  3–2 peak temperature.

#### 4.3. Surrounding cloud material

The envelope of HH 46 is surrounded by cold, quiescent cloud material as evidenced by the LABOCA map and by the CO lines to the south-east (e.g., 20'', –40''). If the cloud is assumed to be isothermal and homogeneous, the CO emission maps from 2–1 to 7–6 can be used to constrain the its properties with the radiative transfer program RADEX (van der Tak et al. 2007)<sup>3</sup>. RADEX calculates the non-LTE excitation and line emission of molecules for a given temperature and density using an escape probability formulation for the radiative transfer. For gas at a constant temperature and density, such as in the surrounding cloud, the results from RADEX and RATRAN are comparable, but RADEX is easier and faster to use. A line width of  $1.2 \text{ km s}^{-1}$  is used from the gaussian fits to the CO 3–2 emission at the cloud positions. The ratios of CO 3–2/6–5 peak temperatures at these cold cloud positions are at least 20, since CO 6–5 is not detected. RADEX simulations show that the CO 6–5 line has to be sub-thermally excited, which can be done when the gas is at low densities or at very low ( $T < 10 \text{ K}$ ) kinetic temperatures. The line ratios are best fitted by a cloud with a temperature of  $\sim 14 \text{ K}$ , a low density of a few times  $10^3 \text{ cm}^{-3}$  and a CO column density of  $10^{17}\text{--}10^{18} \text{ cm}^{-2}$ . The spatial distribution of the CO 3–2 and 6–5 lines also indicate that these cloud conditions extend homogeneously to at least 40'' south of HH 46, the extent of both CO 3–2 and 6–5 maps. Maps of the optically thin  $\text{C}^{18}\text{O}$  3–2, as have been done by van Kempen et al. (2008) for other sources, are needed to further constrain the column density and spatial structure of the surrounding cloud.

## 5. Outflow

### 5.1. Outflow temperature

The spectral line maps clearly reveal the red-shifted outflow to the south-west and the blue-shifted outflow to the north-east. The large difference in extent between the two outflow lobes, already noted by Olberg et al. (1992), is seen in all transitions, with the blue-shifted lobe producing much weaker emission. The brighter and larger outflow lobe seen with *Spitzer* (Noriega-Crespo et al. 2004, Velusamy et al. 2007) corresponds to the red-shifted outflow, which dominates the line profiles of CO. The lack of  $\text{HCO}^+$  outflow wings as well as the absence of  $\text{HCO}^+$  emission in most positions except around the central envelope, suggest that the swept-up gas is at a density of a few times  $10^4 \text{ cm}^{-3}$  or lower.

<sup>3</sup> RADEX is available online at <http://www.sron.rug.nl/~vdtak/radex/radex.php>



**Table 5.** Outflow properties of the red and blue outflow lobe).

| Outflow properties  |                                       |             |                                      |                     |  |  |   |
|---------------------|---------------------------------------|-------------|--------------------------------------|---------------------|--|--|---|
|                     | $V_{\max}^a$<br>(km s <sup>-1</sup> ) | $R$<br>(AU) | $\dot{M}^{b,c}$<br>(M <sub>⊙</sub> ) | $t_d^{a,d}$<br>(yr) | $\dot{M}^{a,e}$<br>(M <sub>⊙</sub><br>yr <sup>-1</sup> ) | $F_{CO}^{b,f}$<br>(M <sub>⊙</sub> yr <sup>-1</sup><br>km s <sup>-1</sup> ) | $L_{\text{kin}}^{b,g}$<br>(L <sub>⊙</sub> ) |
| Red Lobe            |                                       |             |                                      |                     |  |  |   |
| CO 2–1              | 14.2                                  | 5e4         | 0.8/2.9 <sup>h</sup>                 | 2.6e4               | 9.1e-5   | 9.8e-4   | 1.2e-2                                      |
| CO 3–2              | 14.0                                  | >2.5e4      | 0.68                                 | >1.3e4              | 4.2e-5   | 4.5e-4   | 5.4e-3                                      |
| CO 4–3 <sup>i</sup> | 11.0                                  | -           | >0.18                                | -                   | -  | -  | -   |
| CO 6–5              | 10.5                                  | >2.5e4      | 0.48                                 | 2.2e4               | 1.8e-5   | 1.1e-4   | 8.0e-4                                      |
| CO 7–6              | 12.1                                  | 2.0e4       | 0.4                                  | 1.4e4               | 2.2e-5   | 1.7e-4   | 1.6e-3                                      |
| Blue Lobe           |                                       |             |                                      |                     |  |  |   |
| CO 2–1              | 0.5                                   | 1.2e4       | 0.24                                 | 1.2e4               | 1.6e-5   | 9.3e-5   | 6.0e-4                                      |
| CO 3–2              | 0.3                                   | 1.6e4       | 0.24                                 | 1.5e4               | 1.3e-5   | 7.6e-5   | 5.0e-4                                      |
| CO 4–3              | 1.7                                   | 1.1e4       | 0.19                                 | 1.5e4               | 1.1e-5   | 4.5e-5   | 2.2e-4                                      |
| CO 6–5              | 0.5                                   | 1.1e4       | 7e-3                                 | 1.1e4               | 5.4e-7   | 3.0e-6   | 2.0e-5                                      |
| CO 7–6              | 1.1                                   | 1.0e4       | 1e-2                                 | 1.2e4               | 8.6e-7   | 4.3e-6   | 2.4e-5                                      |

<sup>a</sup> Actual LSR velocities; note that the quiescent gas is at  $V_{\text{LSR}}=5.3$  km s<sup>-1</sup>.  $\delta V_{\max}=\text{abs}(V_{\max}-V_{\text{LSR}})$ . Velocities are not corrected for inclination.

<sup>b</sup> Corrected for inclination using the average correction factors of Cabrit & Bertout (1990)

<sup>c</sup> Constant temperature of 100 K assumed for red outflow and 70 K for blue outflow.

<sup>d</sup> Dynamical time scale :  $t_d = R/\delta V_{\max}$

<sup>e</sup> Mass outflow rate :  $\dot{M} = \dot{M}/t_d$ , not corrected for swept-up gas.

<sup>f</sup> Outflow force :  $F_{CO} = M V_{\max}^2 / R$

<sup>g</sup> Kinetic luminosity :  $L_{\text{kin}} = 0.5 M (\delta V_{\max})^3 / R$

<sup>h</sup> 0.8 M<sub>⊙</sub> is derived for a temperature of 50 K. 2.9 M<sub>⊙</sub> is derived for a temperature of 100 K

<sup>i</sup> Outflow extends to far larger scales than map scale.

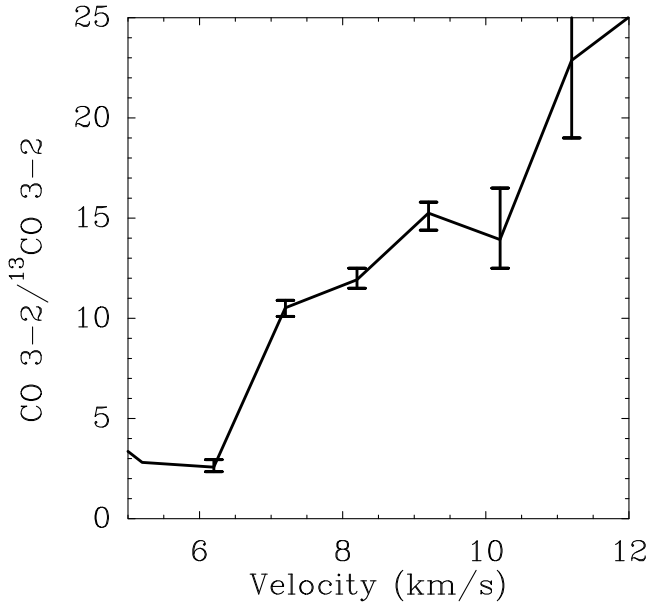


**Fig. 9.** The ratio of the main beam antenna temperatures of <sup>12</sup>CO with respect to <sup>13</sup>CO for the  $J=3-2$  line at the (0,0) position. The ratios correspond to optical depths of 1.8 (ratio of 10) to 1.0 (ratio of 25).

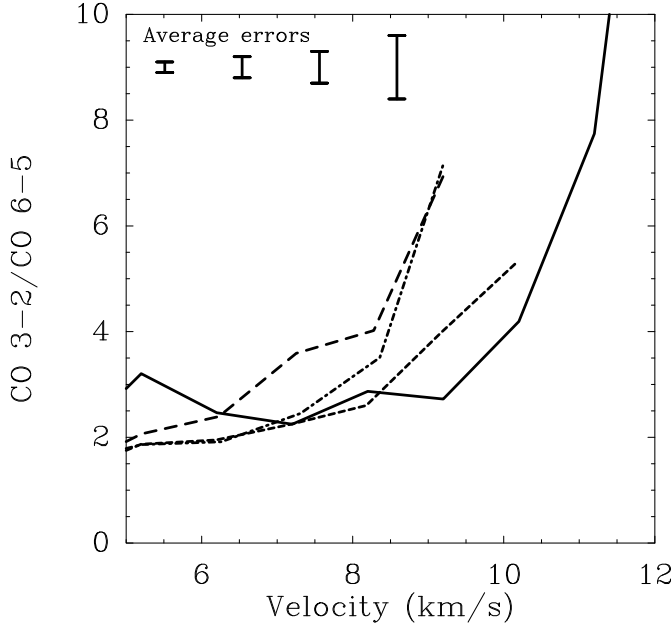
The presence of a strong quiescent component at positions associated with the outflow is discussed in § 6.

The wings of the isotopic lines provide an upper limit to the optical depth,  $\tau_{\text{wing}}$ , of the outflow. The ratio of  $T_{\text{MB}}$  of the <sup>12</sup>CO 3–2/<sup>13</sup>CO 3–2 line wings at the source position is shown in Fig. 9 as a function of velocity. For a constant density of  $3 \times 10^4$  cm<sup>-3</sup> the observed ratios correspond to  $\tau_{\text{wing}}$  of 1.8 (ratio=10) and 1

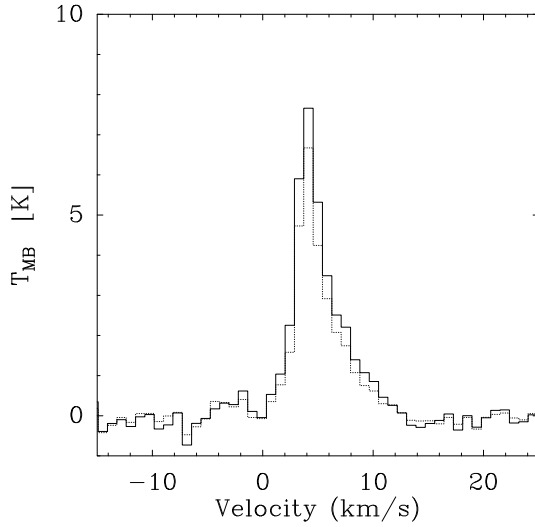
(ratio=25). Fig. 9 shows that the line ratio increases for more extreme velocities, introducing a dependency of  $\tau_{\text{wing}}$  on velocity. In addition, there is a large jump in  $\tau_{\text{wing}}$  from 6 to 7 km s<sup>-1</sup>, representing the transition between the optically thick quiescent and more optically thin shocked material. In the following analysis, it is assumed that all shocked outflow emission (>7 km s<sup>-1</sup>, 1.7 km s<sup>-1</sup> with respect to the systemic velocity of 5.3 km s<sup>-1</sup>) is optically thin for all transitions. The effects of the moderate optical depth of the lines are subsequently discussed.

Fig. 10 shows the ratios of the CO 3–2/6–5 main beam antenna temperatures of line wings as functions of velocity for four different positions along the red outflow axis ((0,0), (-20,-20), (-30,-30) and (-40,-35)). The CO 6–5 data have not been binned to the larger CO 3–2 beam, so the comparison assumes similar volume filling factors of the shocked gas. Figure 11 shows the CO 6–5 spectra binned with a 10'' beam and with a 20'' beam. As can be seen, the differences between the spectra is negligible. Additional testing at other positions confirmed that the spectra do not differ by more than 20%. Ratios are only plotted if the emission in both wings is larger than  $3\sigma$ .

The kinetic temperature  $T_{\text{kin}}$  of the outflow can be derived by comparing the intensity ratios in the line wings from various transitions with model line intensities of van der Tak et al. (2007). With the density assumed to be constant at a few times  $10^4$  cm<sup>-3</sup>, the observed 3–2/6–5 ratios of 2–3 correspond to kinetic temperatures of about 120 to 150 K. Outflow emission is slightly subthermally excited, especially the CO 6–5, with  $T_{\text{ex}}$  ranging from 85 to 120 K. The rising ratios observed at the more extreme velocities in Fig. 10 correspond to lower kinetic temperatures, but even the highest ratios of ~7 still indicate kinetic temperatures greater than 70 K. The variation of the optical depth with velocity, as seen in Fig. 9, could account for the rising ratios seen in Fig. 10, since a higher optical depth will result in a lower ratio for the same temperature. Even with the limit of



**Fig. 10.** The ratio of the  $^{12}\text{CO}$  3–2/ $^{12}\text{CO}$  6–5 main beam antenna temperatures at various positions along the red outflow axis (solid:(0,0), dashed:(-20'',-20''), dot-dashed:(-30'',-30''), long dash:(-40'',-35'')) as functions of velocity. Average error bars at various velocities are given in the upper part of the figure at their respective velocity. They are applicable for all positions except (0,0), for which errors are a factor of 2 lower due to the longer integration time of CO 3–2 at the center position.



**Fig. 11.** The CO 6–5 spectrum at the 0,0 position rebinned at 10'' beam (solid line) and with 20'' (dotted line).

$\tau_{\text{wing}}=1.7$ , the inferred kinetic temperatures will drop by only 20% (see Fig. 4 of Jansen et al. (1996)).

Fig. 12 presents the kinetic temperatures as functions of position along the red outflow for a constant density of  $2 \times 10^4 \text{ cm}^{-3}$ . There is a clear trend towards lower temperatures at larger radii. Averaged between 7 and 9  $\text{km s}^{-1}$ , temperatures drop from 170 K close to the source to 80 K at a distance 40''. However, the error bars, derived from the minimum and maximum ratio at velocities greater than 7  $\text{km s}^{-1}$  show that large variations are pos-

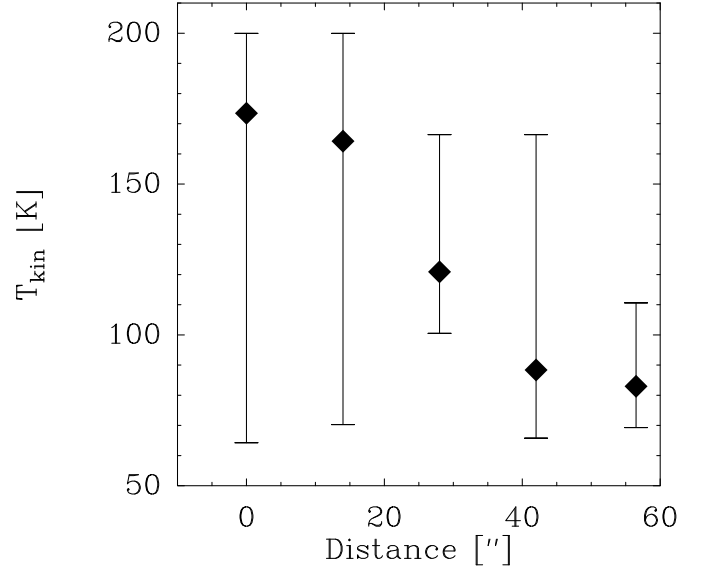


**Fig. 12.** The kinetic temperature of the outflow gas along the red outflow axis computed from the CO 3–2/6–5 line ratio for a constant density of  $2 \times 10^4 \text{ cm}^{-3}$ . Diamonds are the temperatures derived from the velocity-averaged ratios. The limits are determined from the minimum and maximum ratios between 7 and 11  $\text{km s}^{-1}$ . The results are consistent with a constant temperature of  $\sim 100 \text{ K}$  if variations in optical depth and density with distance are taken into account.

sible. In addition to the optical depth effects discussed above, it is also possible that the higher ratios at more extreme velocities and larger distances correspond to lower densities  $n(\text{H}_2)$ . The low density of a few times  $10^3 \text{ cm}^{-3}$  inferred for the surrounding cloud raises the inferred kinetic temperatures from 80 K to 100–120 K. Such a drop in density significantly would lower the  $T_{\text{ex}}$ . The current observational data cannot distinguish between these two possibilities, but both options are consistent with a high kinetic outflow temperature of  $\sim 100 \text{ K}$  that is constant with distance from the source. This temperature is significantly higher than the  $T_{\text{kin}}$  and  $T_{\text{ex}}$  of  $\sim 15 \text{ K}$  assumed by Olberg et al. (1992) for the CO 2–1/1–0 intensity ratios for the HH 46 outflow. Although some studies find  $T_{\text{ex}}$  that low (Bachiller et al. 2001), recent studies, at times including high- $J$  CO, also find higher  $T_{\text{ex}}$  and  $T_{\text{kin}}$  (e.g. Hirano & Taniguchi 2001, Lee et al. 2002). While a cooler outflow component is not excluded, our data clearly show the presence of warmer outflow gas. Kinetic temperatures as low as 50 K would require outflow densities in excess of  $10^5 \text{ cm}^{-3}$ , which are excluded by the  $\text{HCO}^+$  data.

In a similar analysis, the blue-shifted outflow has kinetic temperatures of 70 to 100 K with a lower limit of 50 K, somewhat cooler than the red lobe. In addition to a variation with velocity, the ratios also seem to vary with distance from the source. At larger distances, the CO 3–2/6–5 intensity ratio is almost a factor of 2 higher than at the source position.

Hatchell et al. (1999) use a swept-up shell model to predict kinetic temperatures along the outflow axis and walls. Their predicted values of 50 to 100 K agree very well with our derived temperatures in both outflow lobes (Fig. 12). Such temperatures are much lower than calculated for entrainment models, which predict  $> 1000 \text{ K}$  (e.g., Lizano & Giovanardi 1995). Arce & Goodman (2002) compare different outflow models and show that at least some flows are best explained with the jet-

driven bow shock model. For a thorough review of outflow models, see Arce et al. (2007). The models from Hatchell et al. (1999) predict an almost constant temperature along most of the outflow axis with increasing temperatures near the bow shock, the main site of energy deposition. This is consistent with our constant temperature along the outflow axis.

## 5.2. Other outflow properties

Additional properties of both outflow lobes are derived from the molecular emission maps following the recipe outlined in Hogerheijde et al. (1998), in which the radii, masses, dynamical time scales, outflow force and kinetic luminosity are calculated (see Table 5). The results are corrected for the inclination of  $35^\circ$  found for this source (Reipurth & Heathcote 1991, Micono et al. 1998) using an average of the three correction factors from Cabrit & Bertout (1990) (their Figures 5–7). These factors range from 1.2 to 2.5, especially for the mass, and are introduced to account for the difference in observed  $V_{\max}$  on the sky and the actual extreme velocities. Although excitation temperature variations are seen throughout the outflow that depend on velocity and distance from the source, we assume an average excitation temperature of 100 K for the red outflow lobe and 70 K for the blue outflow lobe for the derivation of these parameters.

The resulting values can be uncertain up to an order of magnitude due to the variations in the covered area and thus in radius, especially for the CO 4–3 (observed with FLASH). The mass estimates of the low excitation CO lines (e.g., the CO 2–1) may be overestimated by up to a factor 4, due to the larger area covered and the assumption that the outflow is iso-thermal at 100 K. CO 2–1 may be dominated by cooler gas with temperatures down to, say, 50 K, lowering the mass estimate to a lower limit  $0.8 M_\odot$ , only 25% higher than the masses found for the high- $J$  CO lines. Temperature differences are likely also responsible for the (smaller) difference in masses in the other lines.

Even with the uncertainties in covered area, the dynamical time scales for these outflows all converge on 10,000 to 20,000 years, with no difference between the red and blue outflow lobes. The values of Table 5 are similar to the results found in Cabrit & Bertout (1992) and Hogerheijde et al. (1998) for other Class I outflows and also agree with the results from Olberg et al. (1992) who find  $L_{\text{kin}} = 4.5 \times 10^{-3} L_\odot$  and dynamical time scales of  $4 \times 10^4$  yr. Although our dynamical time scales are a factor of 2 smaller, this can be accounted for by the smaller covered area in our observations.

The main discrepancy with older studies is that our outflow mass is up to an order of magnitude higher than that by Olberg et al. (1992). The origin of this difference is two-fold. First, Olberg et al. (1992) do not apply correction factors from Cabrit & Bertout (1990). Second, there is a large difference between assumed temperatures in the red lobe (15 K vs 100 K). Although Olberg et al. (1992) derive their temperature from the CO 1–0 and 2–1 emission, the presence and intensity of CO 4–3, 6–5 and 7–6 outflow emission strongly constrain temperatures to our higher value of 100 K. As illustrated by the CO 2–1 example, this can introduce a significant difference in the masses.

At first sight, there is no difference with the masses derived by Chernin & Masson (1991), but they assumed a similar temperature of 15–30 K as Olberg et al. (1992). However, Chernin & Masson (1991) took an optical depth of  $\sim 5$  for the outflow emission, which is not confirmed by our observed lack of outflow emission in the  $^{13}\text{CO}$  lines. For our observed maxi-

mum  $\tau_{\text{wing}} = 1.7$ , the outflow mass as derived from CO 3–2 would increase by a factor of 2 ( $\approx \tau/(1 - e^{-\tau})$ ).

From the dust map, a total (envelope + cloud) mass of  $8 M_\odot$  is derived (see § 5.3.2). The total outflow mass in Table 5 can be as high as  $3.2 M_\odot$  and thus consist of a significant portion (40%) of that total mass. If the low mass for CO 2–1 is adopted, this percentage drops to 10%.

Bontemps et al. (1996) empirically derive a relation between the flow force,  $F_{\text{CO}}$  and bolometric luminosity

$$\log(F_{\text{CO}}) = 0.9 \log(L_{\text{bol}}) - 5.6 \quad (1)$$

and the envelope mass

$$\log(F_{\text{CO}}) = 1.1 \log(M_{\text{env}}) - 4.15 \quad (2)$$

Using the bolometric luminosity of  $16 L_\odot$  and envelope mass of  $\sim 5 M_\odot$ , flow forces of between  $3 \times 10^{-5}$  and  $4 \times 10^{-4} M_\odot \text{ yr}^{-1} \text{ km s}^{-1}$  are expected. The parameters for the red outflow lobe indeed show flow forces for most CO transitions that agree with these predictions. Only the flow force of CO 2–1 is a factor of 2.5 higher. If the lower mass of  $0.8 M_\odot$  is used for this transition due to a lower outflow temperature of 50 K, the flow force similarly drops by a factor of 3.5, almost identical to the flow forces found for the CO 6–5 and 7–6.

The observed flow forces for the blue outflow lobe are up to two orders of magnitude lower than those of the red lobe. This ‘missing’ outflow force can be explained by assuming that the blue-shifted outflow escapes the envelope and surrounding cloud and thus interacts much less with the surrounding cloud due to a lack of cloud material in the path of this outflow lobe.

## 6. Origin of the quiescent high- $J$ CO line emission

### 6.1. Photon heating of cavity walls

The analysis in § 4.2 shows that an envelope model derived from the dust emission is not able to fit the quiescent emission of the high-excitation lines by a factor of  $\sim 2.5$ , even though the low-excitation optically thin lines are well-fitted with standard abundances. The limits on the  $\text{C}^{18}\text{O}$  6–5, combined with the information that the  $^{12}\text{CO}$  6–5 emission from the envelope is optically thick, implies that an additional heating component must be present that produces quiescent emission. There are several constraints on this component. First, it cannot originate in the inner regions of the protostellar envelope or be obscured by the envelope itself, because emission from such a component cannot escape through the optically thick outer envelope emission. Second, it must be (nearly) optically thin, since the observed  $\text{C}^{18}\text{O}$  6–5 limit is already reached by the envelope itself. Thus, it cannot contribute significantly in mass. Third, it must be extended since a similar warm quiescent component is also clearly seen at other positions covering the red-shifted outflow through narrow  $^{12}\text{CO}$  6–5 emission, e.g. at positions ( $-20''10''$ ) and ( $-20''$ ,  $-20''$ ) (see Fig. 6 and 5). Observations of  $^{13}\text{CO}$  6–5 at other positions also confirm that this quiescent emission cannot be very optically thick ( $\tau < 0.4$ ).

Spaans et al. (1995) investigated the influence of photon heating on the emission of high- $J$  CO lines, in order to explain the bright but narrow  $^{12}\text{CO}$  and  $^{13}\text{CO}$  6–5 single spectra observations of Class I sources (Hogerheijde et al. 1998). In this process ultraviolet (UV) photons heat the gas of the outflow cavity walls to temperatures of a few hundred K, but are unable to dissociate the CO molecules. The photons in this model originate in a  $\sim 10,000$  K radiation field of the boundary layer in the accretion disk. It was proposed that dust present in the cavity scatters

the UV photons towards the cavity walls. The turbulent velocity of the gas at the cavity walls is low, thus explaining the narrow width of the CO 6–5 and 7–6 lines. This extra warm gas due to photon heating could account for the differences in the observed  $^{12}\text{CO}$  and  $^{13}\text{CO}$  6–5 emission on source and that modelled by just a protostellar envelope.

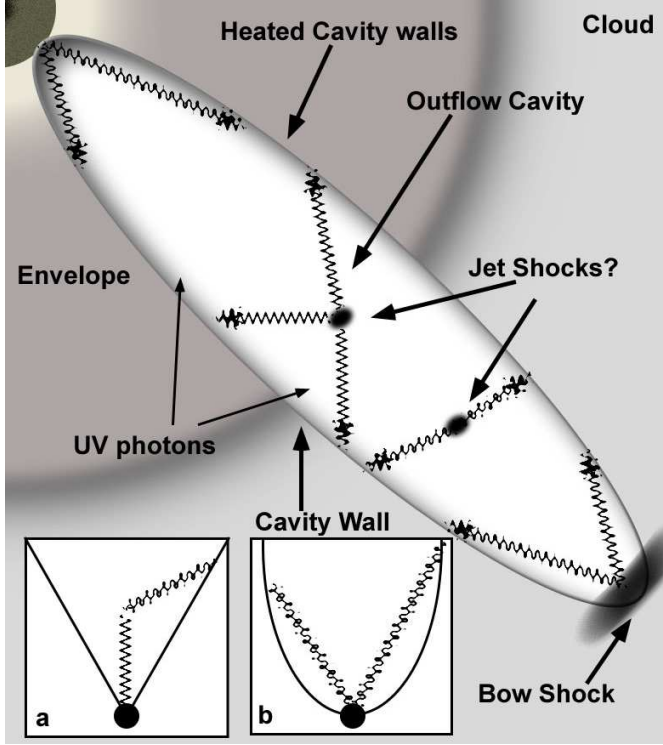


**Fig. 13.** Cartoon model of the HH 46 outflow on scales up to the bow shock ( $\sim 60,000 \text{ AU} \times \sim 60,000 \text{ AU}$ ), illustrating the photon heating of the cavity walls that is responsible for the high- $J$  CO emission. UV photons are created both in the accretion disk boundary layer, as well as the bow shock and illuminate the cavity walls. Illustrative paths of the UV photons are shown with wiggly lines. In inset **a**, the method of photon heating proposed by Spaans et al. (1995) using an outflow with constant opening angle is shown. There, dust must scatter UV photons to produce significant irradiation of the cavity walls. In inset **b**, a parabolic shape of the outflow cavity allows many more UV photons to directly impact the outflow cavity walls. Due to the expected long mean free path of UV photons within the outflow cavity ( $\sim 65,000 \text{ AU}$ ), scenario **b** is assumed to be the more likely scenario. See the text for more information.

Although Spaans et al. (1995) only include photons created in the accretion disk and thus limit their Photon Dominated Region (PDR) to a central region of up to 4,000 AU in size, this model can be extended if additional sources of UV photons are included. Such photons can be produced at bow shock positions of the outflow if  $J$ -shocks are present there (Neufeld & Dalgarno 1989). Such photons can also heat the dust at the cavity walls, increasing the emission of the dust particles at continuum wavelengths as presented in Fig. 2. The elongated continuum emission of HH46 on a  $1'$  scale in the south-east direction may indeed be caused by warm dust, instead of more massive cold dust or CO emission. Velusamy et al. (2007) show that apart from the  $24 \mu\text{m}$  hotspot of HH 47C, two additional  $24 \mu\text{m}$  emission spots can

be found within the outflow cavity of HH 46/47, that likely originate in the jet (see Fig. 3 in Velusamy et al. 2007). These positions produce additional UV photons, creating a much more extended PDR. The bow shock at the position of HH 47C, the two new jet/shock positions and the accretion shock boundary layer combined are excellent sources of the necessary UV photons. Figure 13 shows a schematic overview of the red-shifted outflow cavity and the proposed process of photon heating within the HH 46/47 outflow. § 6.2 discusses the path of the UV photons in more detail, while § 6.3 presents the constraints on the UV field.

### 6.2. Importance of the outflow geometry

To illuminate a larger area of the cavity wall than possible by direct irradiation Spaans et al. (1995) invoked scattering of the UV photons by the dust present in the outflow cavity, even though such scattering is dominated by anisotropic, mainly forward scattering. With a constant opening angle (see inset **a** of Fig. 13), only a very small area of the envelope wall will be directly impacted by UV photons. However, with densities of a few  $100 \text{ cm}^{-3}$  the mean free path of a UV photon until its first scattering event is  $\sim 65,000 \text{ AU}$ , with the assumption that on average an  $A_V$  of 1 produces a single scattering event (Draine 2003). This is significantly larger ( $\sim 150''$  on the sky) than the area covered by the outflow cavity.

A parabolic shape of the outflow cavity in the regions near the envelope, as seen in inset **b** of Fig. 13, allows much more UV radiation from the accretion boundary layer to illuminate the cavity walls at larger distances of a few thousand AU. A more quantitative description of outflow shapes and its effect on the illumination of the outflow walls is beyond the scope of this paper.

### 6.3. Constraining the UV field

The temperature of the cavity walls can be derived from the radiation field originating from these shocks. The radiation field  $G_0$  at the cavity walls can be characterized by

$$G_0 = \sum G_0^i f^i \quad (3)$$

with  $G_0^i$  the radiation field originating at each shock position  $i$  and  $f^i$  a geometric dilution factor to account for the difference in the UV emitting surface to the total illuminated surface of the cavity walls. A dissociative shock  $i$  produces  $3 \times 10^7 (v_s/100 \text{ km s}^{-1})^3 (n_0)$  photons  $\text{cm}^{-2} \text{ s}^{-1}$  assuming all energy is emitted at 10 eV (Neufeld & Dalgarno 1989). This is equivalent of a  $G_0^i$  of 30,000 assuming a density  $n_0$  of  $10^4 \text{ cm}^{-3}$  and a shock velocity  $v_s$  of  $220 \text{ km s}^{-1}$ , derived for the bow shock (Fernandes 2000). The average factor of  $f^i$  over all shocks is assumed to be 0.005, meaning that the working surface of each shock is  $\sim 1/200$  in size compared to the cavity surface. However, not all shocks will have a velocity as high as  $220 \text{ km s}^{-1}$ . It is more likely that the velocities of the secondary shocks within the cavity are much lower. But similarly, the size of the working surfaces of the shocks, and thus the  $f^i$  can be larger, resulting in a comparable overall strength  $G_0$ , but of a different ‘color’. With four spots, the cavity walls are illuminated by a total  $G_0$  equaling  $\sim 600$  with an uncertainty of a factor of 2 to 3 due to the uncertainty in the  $f^i$ . Using the results from Kaufman et al. (1999, their Figure 1), the PDR surface temperature is then constrained to 250–400 K, sufficient to produce the observed lines.

[C I] 2–1 is detected near and at the bow shock position, but not at the outflow positions closer to the star, although the dynamic range in the [C I] data is small. This could indicate that the penetrating UV photons within the region of the outflow lobe closer to the star are not able to dissociate CO significantly, constraining the color temperature of the radiation field. Neufeld & Dalgarno (1989) show that shocks with velocities less than  $90 \text{ km s}^{-1}$  do not produce CO dissociating photons. If all shocks have  $v_s \approx 80 \text{ km s}^{-1}$  the estimated  $G_0^i$  drops by a factor  $\sim 20$ . In that case, the total  $G_0$  is not sufficient to heat the cavity walls to surface temperatures of 250–400 K, but only to about 100 K. Lower velocities are likely for the shocks observed inside the cavity. However, the known shock velocity of  $220 \text{ km s}^{-1}$  (Fernandes 2000) is sufficient to produce CO dissociating photons, consistent with the observed narrow [C I] emission at this position. This situation is reminiscent of the observation of strong quiescent [C I] 1–0 emission in the supernova remnant IC 443 ahead of the shock, originating from photodissociation of CO in the pre-shocked gas (Keene et al. 1996). The likely scenario for HH 46 is thus

1. Non-dissociative UV photons are created in the boundary layer and secondary shocks, while the bow shock produces mainly CO dissociative UV photons
2. Along the outflow axis, the cavity walls are heated to sufficient temperatures to produce the quiescent high- $J$  CO emission.
3. Closer to the bow shock, dissociation of CO becomes significant in addition to the heating of the cavity walls, explaining the lack of CO 6–5 emission and presence of [C I] 2–1 emission near and at the bow shock

Observations of far-IR CO lines, such as are possible with the *HIFI* and *PACS* instruments on *Herschel*, are needed to constrain the exact temperature of CO gas at the cavity walls.

Slow ( $v_s = 5\text{--}10 \text{ km s}^{-1}$ ) C-type shocks along the outflow cavity walls are able to generate similar amounts of CO emission (Draine & Roberge 1984). However, the narrow nature of the line profile, as well as the presence of CO 6–5 emission over the entire area traced by the IR outflow, make this scenario less likely than the photon heating, although it could contribute some.

## 7. Conclusions

In this paper, we characterize the structure of protostellar envelope and the molecular outflow associated with HH 46 IRS 1, as well as its immediate surrounding cloud material, through dust and molecular line maps. Broad and narrow CO lines are observed ranging in transitions from 2–1 to 7–6, including isotopologues. The three distinct components can be best described by the following model:

- **Envelope** - The envelope of HH 46 with  $\sim 3\text{--}5 M_\odot$  (within  $T > 10 \text{ K}$ ) is one of the most massive ones found for a Class I low-mass protostar, but is densely concentrated toward the center ( $n \propto r^{-1.8}$ ). The  $\text{C}^{18}\text{O}$  line emission from the envelope can be best fitted with a drop abundance of  $2.7 \times 10^{-4}/1 \times 10^{-5}$  above/below 30 K and below/above  $10^5 \text{ cm}^{-3}$ . However, such abundances are unable to reproduce the observed  $^{12}\text{CO}$  and  $^{13}\text{CO}$  6–5 and 7–6 emission. The dense envelope itself is best traced by the  $\text{HCO}^+$  4–3 emission, which has very little outflow contribution and shows a spherical distribution. Densities in the inner few hundred AU of the envelope are high ( $> 10^7 \text{ cm}^{-3}$ ), with high optical depths

of the  $\text{HCO}^+$  4–3 and all  $^{12}\text{CO}$  lines. A  $\text{C}/\text{H}_2$  abundance of a few times  $10^{-7}$  is found, which can be maintained by photodissociation of CO by cosmic ray induced UV photons.

- **Surrounding cloud** - The surrounding cloud extends over more than  $100''$  to the south-southwest but does not extend further than  $\sim 30''$  north of HH 46 IRS 1 where even no low excitation CO emission is found. Cloud conditions include a low density of a few times  $10^3 \text{ cm}^{-3}$ , derived from limits on the CO 6–5 emission at positions such as  $(30'', -20'')$ . The total column of CO is  $\sim 10^{18} \text{ cm}^{-2}$ .
- **Outflow** - The red-shifted molecular outflow, extending at least  $40''$  from the source, produces strong molecular line wings up to CO  $J=7\text{--}6$  and heats the surrounding cloud and envelope significantly close to the star. Spatially, the red-shifted outflow lobe corresponds to the bright infrared outflow lobe from Noriega-Crespo et al. (2004). Optical depth of the CO 3–2 outflow wing is less than 1.7. Kinetic temperatures of the red-shifted outflow are of order 100–150 K close to the star for flow densities of  $2 \times 10^4 \text{ cm}^{-3}$ , but drop to 80 K further from the central source if densities and optical depth remain constant. However, the data are also consistent with a constant kinetic temperature in the covered area if densities decrease to a few  $10^3$  at a distance  $> 40''$  from the central source, as found for the surrounding cloud.

Temperatures of both outflow lobes are significantly higher than the previously derived temperature of 15 K, but agree well with the model predictions of Hatchell et al. (1999) for a swept-up shell model. The high temperature causes the observed outflow mass to be significantly higher (almost an order of magnitude) than derived in older studies such as Olberg et al. (1992). Bright narrow [C I] is found near the bow shock, indicating that the bow shock produces CO dissociating photons.

- **Origin of high- $J$  CO** - The emission seen in the higher excitation CO transition has three main origins.
  1. The dense envelope produces optically thick emission in both CO 6–5 and 7–6, originating in the warm ( $T > 50 \text{ K}$ ) inner envelope, accounting for roughly 1/3 of the observed line intensities on source.
  2. High- $J$  CO emission is detected in the red- and blue-shifted outflow wings at some positions along the outflow axis.
  3. The bulk of the high- $J$  CO emission has narrow lines and is produced by photon heating. UV photons originating in the bow shocks, jet shocks and accretion boundary layer heat the cavity walls up to a few hundred K. The lack of strong associated [C I] emission near the source indicates that the UV photons do not photodissociate CO, suggesting shock velocities lower than  $90 \text{ km s}^{-1}$  such as could be present inside the cavity. CO dissociating photons are limited to the region close to the bow shock.

This paper shows that the addition of the high- $J$  CO emission lines as observed with CHAMP<sup>+</sup> provides new insights into the physical structure of the protostellar envelope and molecular outflow of HH 46. The presence of narrow line emission in the high- $J$  CO lines throughout the outflow suggests that photon heating is an important process in HH 46. The high- $J$  isotopic CO lines, in particular those of  $\text{C}^{18}\text{O}$  6–5, have been key in constraining the envelope model. The UV radiation implied by the high- $J$  CO and [C I] observations should also have significant

consequences for the chemistry of other species and should enhance radicals like CN and OH along the outflow walls. Future high-frequency observations using high- $J$  CHAMP<sup>+</sup>, Herschel and, in the long run, ALMA high frequency bands, will provide unique constraints on the interaction between outflow and envelope.

*Acknowledgements.* TvK and astrochemistry at Leiden Observatory are supported by a Spinoza prize and by NWO grant 614.041.004. CHAMP<sup>+</sup> is built with NWO grant 600.063.310.10. TvK is grateful to the APEX staff for carrying out the bulk of the low-frequency observations. Carlos de Breuck is thanked for providing the APEX-1 observations on a very short notice within the science verification project E-81.F-9837A. We appreciate the input of Steve Doty into an illuminating and essential discussion about outflow cavity shapes. We are grateful for support from Ronald Stark throughout construction of CHAMP<sup>+</sup>. Constructive comments by an anonymous referee helped improve the paper.

## References

- Arce, H. G. & Goodman, A. A. 2002, *ApJ*, 575, 928
- Arce, H. G., Shepherd, D., Gueth, F., et al. 2007, in *Protostars and Planets V*, ed. B. Reipurth, D. Jewitt, & K. Keil, 245–260
- Bachiller, R., Pérez Gutiérrez, M., Kumar, M. S. N., & Tafalla, M. 2001, *A&A*, 372, 899
- Blake, G. A., Sandell, G., van Dishoeck, E. F., et al. 1995, *ApJ*, 441, 689
- Bontemps, S., Andre, P., Terebey, S., & Cabrit, S. 1996, *A&A*, 311, 858
- Boogert, A. C. A., Hogerheijde, M. R., Ceccarelli, C., et al. 2002, *ApJ*, 570, 708
- Cabrit, S. & Bertout, C. 1990, *ApJ*, 348, 530
- Cabrit, S. & Bertout, C. 1992, *A&A*, 261, 274
- Ceccarelli, C., Castets, A., Caux, E., et al. 2000, *A&A*, 355, 1129
- Ceccarelli, C., Hollenbach, D. J., & Tielens, A. G. G. M. 1996, *ApJ*, 471, 400
- Chernin, L. M. & Masson, C. R. 1991, *ApJ*, 382, L93
- Di Francesco, J., Johnstone, D., Kirk, H., MacKenzie, T., & Ledwosinska, E. 2008, *ApJS*, 175, 277
- Dopita, M. A., Evans, I., & Schwartz, R. D. 1982, *ApJ*, 263, L73
- Doty, S. D. & Neufeld, D. A. 1997, *ApJ*, 489, 122
- Draine, B. T. 2003, *ApJ*, 598, 1017
- Draine, B. T. & Roberge, W. G. 1984, *ApJ*, 282, 491
- Fernandes, A. J. L. 2000, *MNRAS*, 315, 657
- Flower, D. R., Le Boulrot, J., Pineau Des Forets, G., & Roueff, E. 1994, *A&A*, 282, 225
- Güsten, R., Baryshev, A., Bell, A., et al. 2008, in *Society of Photo-Optical Instrumentation Engineers (SPIE) Conference Series*, Vol. 7020, Society of Photo-Optical Instrumentation Engineers (SPIE) Conference Series
- Güsten, R., Nyman, L. Å., Schilke, P., et al. 2006, *A&A*, 454, L13
- Hatchell, J., Fuller, G. A., & Ladd, E. F. 1999, *A&A*, 344, 687
- Heathcote, S., Morse, J. A., Hartigan, P., et al. 1996, *AJ*, 112, 1141
- Henning, T., Pfau, W., Zinnecker, H., & Prusti, T. 1993, *A&A*, 276, 129
- Hirano, N. & Taniguchi, Y. 2001, *ApJ*, 550, L219
- Hogerheijde, M. R. & van der Tak, F. F. S. 2000, *A&A*, 362, 697
- Hogerheijde, M. R., van Dishoeck, E. F., Blake, G. A., & van Langevelde, H. J. 1998, *ApJ*, 502, 315
- Ivezić, Z. & Elitzur, M. 1997, *MNRAS*, 287, 799
- Jansen, D. J., van Dishoeck, E. F., Keene, J., Boreiko, R. T., & Betz, A. L. 1996, *A&A*, 309, 899
- Jørgensen, J. K., Lahuis, F., Schöier, F. L., et al. 2005a, *ApJ*, 631, L77
- Jørgensen, J. K., Schöier, F. L., & van Dishoeck, E. F. 2002, *A&A*, 389, 908
- Jørgensen, J. K., Schöier, F. L., & van Dishoeck, E. F. 2005b, *A&A*, 437, 501
- Kasemann, C., Güsten, R., Heyminck, S., et al. 2006, Presented at the Society of Photo-Optical Instrumentation Engineers (SPIE) Conference, 6275
- Kaufman, M. J., Wolfire, M. G., Hollenbach, D. J., & Luhman, M. L. 1999, *ApJ*, 527, 795
- Keene, J., Phillips, T. G., & van Dishoeck, E. F. 1996, in *IAU Symposium*, Vol. 170, CO: Twenty-Five Years of Millimeter-Wave Spectroscopy, ed. W. B. Latter, J. E. Radford Simon, P. R. Jewell, J. G. Mangum, & J. Bally, 382–
- Klein, B., Philipp, S. D., Krämer, I., et al. 2006, *A&A*, 454, L29
- Kreysa, E., Bertoldi, F., Gemuend, H.-P., et al. 2003, Presented at the Society of Photo-Optical Instrumentation Engineers (SPIE) Conference, 4855, 41
- Lee, C.-F., Mundy, L. G., Stone, J. M., & Ostriker, E. C. 2002, *ApJ*, 576, 294
- Lizano, S. & Giovanardi, C. 1995, *ApJ*, 447, 742
- Maret, S., Ceccarelli, C., Caux, E., et al. 2004, *A&A*, 416, 577
- Micono, M., Davis, C. J., Ray, T. P., Eisloffel, J., & Shetrone, M. D. 1998, *ApJ*, 494, L227+
- Neufeld, D. A. & Dalgarno, A. 1989, *ApJ*, 340, 869
- Nisini, B., Giannini, T., & Lorenzetti, D. 2002, *ApJ*, 574, 246
- Noriega-Crespo, A., Morris, P., Marleau, F. R., et al. 2004, *ApJS*, 154, 352
- Olberg, M., Reipurth, B., & Booth, R. S. 1992, *A&A*, 259, 252
- Parise, B., Belloche, A., Leurini, S., et al. 2006, *A&A*, 454, L79
- Raymond, J. C., Morse, J. A., Hartigan, P., Curiel, S., & Heathcote, S. 1994, *ApJ*, 434, 232
- Reipurth, B. & Heathcote, S. 1991, *A&A*, 246, 511
- Schöier, F. L., Jørgensen, J. K., van Dishoeck, E. F., & Blake, G. A. 2002, *A&A*, 390, 1001
- Schöier, F. L., van der Tak, F. F. S., van Dishoeck, E. F., & Black, J. H. 2005, *A&A*, 432, 369
- Schwartz, R. D. 1977, *ApJS*, 35, 161
- Schwartz, R. D. & Greene, T. P. 2003, *AJ*, 126, 339
- Shirley, Y. L., Evans, N. J., Rawlings, J. M. C., & Gregersen, E. M. 2000, *ApJS*, 131, 249
- Siringo, G., Kreysa, E., Kovacs, A., et al. 2008, in *Society of Photo-Optical Instrumentation Engineers (SPIE) Conference Series*, Vol. 7020, Society of Photo-Optical Instrumentation Engineers (SPIE) Conference Series
- Spaans, M., Hogerheijde, M. R., Mundy, L. G., & van Dishoeck, E. F. 1995, *ApJ*, 455, L167+
- Stanke, T., McCaughrean, M. J., & Zinnecker, H. 1999, *A&A*, 350, L43
- van der Tak, F. F. S., Black, J. H., Schöier, F. L., Jansen, D. J., & van Dishoeck, E. F. 2007, *A&A*, 468, 627
- van Dishoeck, E. F., Blake, G. A., Jansen, D. J., & Groesbeck, T. D. 1995, *ApJ*, 447, 760
- van Kempen, T. A., Doty, S. D., van Dishoeck, E. F., Hogerheijde, M. R., & Jørgensen, J. K. 2008, *A&A*, 487, 975
- van Kempen, T. A., Hogerheijde, M. R., van Dishoeck, E. F., et al. 2006, *A&A*, 454, L75
- Velusamy, T., Langer, W. D., & Marsh, K. A. 2007, *ApJ*, 668, L159
- Walker, C. K., Narayanan, G., Buettgenbach, T. H., et al. 1993, *ApJ*, 415, 672
- Wilson, T. L. & Rood, R. 1994, *ARA&A*, 32, 191